# All-Perovskite Tandem Photovoltaics: Present Status and Future Opportunities

Jin Wen[1]†, Hang Hu[2,3]†, Chao Chen[4]†, David P. McMeekin[5]†, Ke Xiao[1], Renxing Lin[1], Ye Liu[6], Henry J. Snaith[5]*, Jiang Tang[4]*, Ulrich W. Paetzold[2,3]* and Hairen Tan[1,6]*

[1]*National Laboratory of Solid State Microstructures, Frontiers Science Center for Critical Earth Material Cycling, College of Engineering and Applied Sciences, Nanjing University, Nanjing 210023, China*

[2]*Institute of Microstructure Technology (IMT), Karlsruhe Institute of Technology (KIT), Hermann-von-Helmholtz-Platz 1, 76344 Eggenstein-Leopoldshafen, Germany*

[3]*Light Technology Institute (LTI), Karlsruhe Institute of Technology (KIT), Engesserstrasse 13, 76131 Karlsruhe, Germany*

[4]*Wuhan National Laboratory for Optoelectronics (WNLO) and School of Optical and Electronic Information, Huazhong University of Science and Technology (HUST), Wuhan, Hubei, China.*

[5]*Clarendon Laboratory, Department of Physics, University of Oxford, Oxford, UK.*

[6]*Research and Development Center, Renshine Solar (Suzhou) Co., Ltd, Changshu, Suzhou, China.*

† These authors contributed equally to this work.

*Corresponding authors. E-mails: hairentan@nju.edu.cn; ulrich.paetzold@kit.edu; jtang@mail.hust.edu.cn; henry.snaith@physics.ox.ac.uk

**All-perovskite tandem solar cells represent the forefront of next-generation photovoltaic technologies, offering a promising pathway to exceed the Shockley-Queisser efficiency limits of single-junction solar cells, while maintaining cost-effectiveness and scalability. However, transitioning from lab-scale prototypes to commercially viable products faces numerous challenges. Large-area fabrication requires developing scalable manufacturing techniques while minimizing performance losses compared to laboratory-scale spin-coating. Additionally, achieving long-term stability, reliability, efficient integration from cell to module, and high yield during practical deployment remain critical hurdles. This review addresses these key aspects, summarizes the latest field advancements, and highlights**

**strategies to overcome these challenges. By offering insights into the pathway toward reliable, durable, and high-performance all-perovskite tandem photovoltaics, this review aims to support their deployment in large-scale applications.**

## Introduction

The photovoltaic (PV) industry has witnessed remarkable progress in recent years, driven by significant cost reductions, efficiency improvements, and extended system lifetimes, making it one of the most competitive renewable energy sources. However, as silicon-based PV technologies mature, their record efficiency of 27.4% for crystalline silicon (c-Si) cells is nearing their practical theoretical limits of ~29.4%[1], leaving limited room for substantial efficiency gains within the c-Si PV technologies.

To overcome this limitation and further reduce the levelized cost of electricity (LCOE) for PV electricity generation, a multi-junction architecture approach exceeding the efficiency limit of single-junction devices is highly demanded[2]. A promising pathway towards this goal utilizes all-perovskite tandem solar cells, which leverage the ability of perovskite materials to flexibly tune their band gaps. This material property allows for two or more subcells with complementary bandgaps to be integrated into one solar cell device[3]. This technology benefits from a reduction in photon thermalization losses, allowing for record certified power conversion efficiencies (PCEs) reaching beyond 30%, thus, outperforming single-junction silicon (27.4%) and perovskite (26.7%) solar cells[1]. Moreover, the certified mini-module efficiencies for all-perovskite tandems have reached 24.8%, surpassing the 23.2% efficiency of single-junction perovskite modules[1].

Beyond their exceptional efficiency, all-perovskite tandem solar cells benefit from abundant precursor materials, low-energy production and vapor or solution-processable fabrication, positioning them as a cost-effective alternative to Si-based PV. While perovskite-Si tandem cells have achieved efficiencies of 34.6%[1], all-perovskite tandems have even higher theoretical limits[4]. Moreover, the capabilities to manufacture tandem cells using low-temperature and scalable processing methods allow for diverse applications, ranging from lightweight and flexible panels to building-integrated photovoltaics. Combined with their potential for further efficiency gains, these unique properties position all-perovskite tandems as a pivotal technology for large-scale solar energy deployment. However, transitioning from laboratory prototype cells to commercially

viable module products requires overcoming critical scalability, stability, and real-world reliability challenges.

This review provides a comprehensive overview of recent progress in all-perovskite tandem solar cells, focusing on strategies to improve the efficiency and address challenges in stability and scalability. It examines the mechanisms driving efficiency improvements, emphasizing the unique features and critical challenges of the p-i-n (positive-intrinsic-negative) architecture, also known as the "inverted" architecture of the wide-bandgap (WBG) and narrow-bandgap (NBG) subcells. It further explores material and structural factors influencing tandem stability, with a focus on emerging methodologies to improve durability. The next discussion extends to the transition from small-area devices to large-area modules, highlighting bottlenecks in large-area processing. Finally, the review suggests key directions for future research, offering a roadmap to advance all-perovskite tandem solar cells toward practical applications.

**BOX 1| Typical device architecture of all-perovskite tandem solar cells**

All-perovskite tandem solar cells are classified into two main architectures: two-terminal (2T) and four-terminal (4T). The 4T design employs optical splitting or mechanical stacking, enabling each subcell to operate electrically independently (**Fig. 1a**). While this structure offers resilience towards spectral variations, it incurs a greater complexity and higher production costs, compared to 2T tandem solar cells, due to additional transparent electrodes and interconnection component. In contrast, the 2T architecture integrates both subcells into a monolithic stack with an interconnected tunnel recombination junction (TRJ), requiring a precise current matching for maximizing power output. This simple design facilitates integration into existing module frameworks and lowers production costs. However, its reliance on current matching can significantly limit the efficiency of the overall tandem if either subcell is considerably less efficient than intended. Additionally, stacking more than ten layers increases the complexity of the fabrication process, potentially reducing the production yield of the device. This results in the need for tight industrial and manufacturing processes.

The TRJ, typically composed of materials like metal oxides (*e.g.*, $MoO_x$, ITO) or ultrathin metal nanoclusters, enables efficient recombination between electrons (photo-generated from the top cell) and holes (photo-generated from the bottom cell) (**Fig. 1b**). For realizing an efficient performance, the TRJ needs high vertical conductivity while minimizing lateral conductivity to prevent shunting.

Ideally, the tandem device's open-circuit voltage ($V_{OC}$) equals of the $V_{OC}$ of each subcell with minimal fill factor (FF) loss[5]. Additionally, the TRJ requires high optical transmittance to minimize reflection and parasitic absorption losses, ensuring efficient light harvesting.

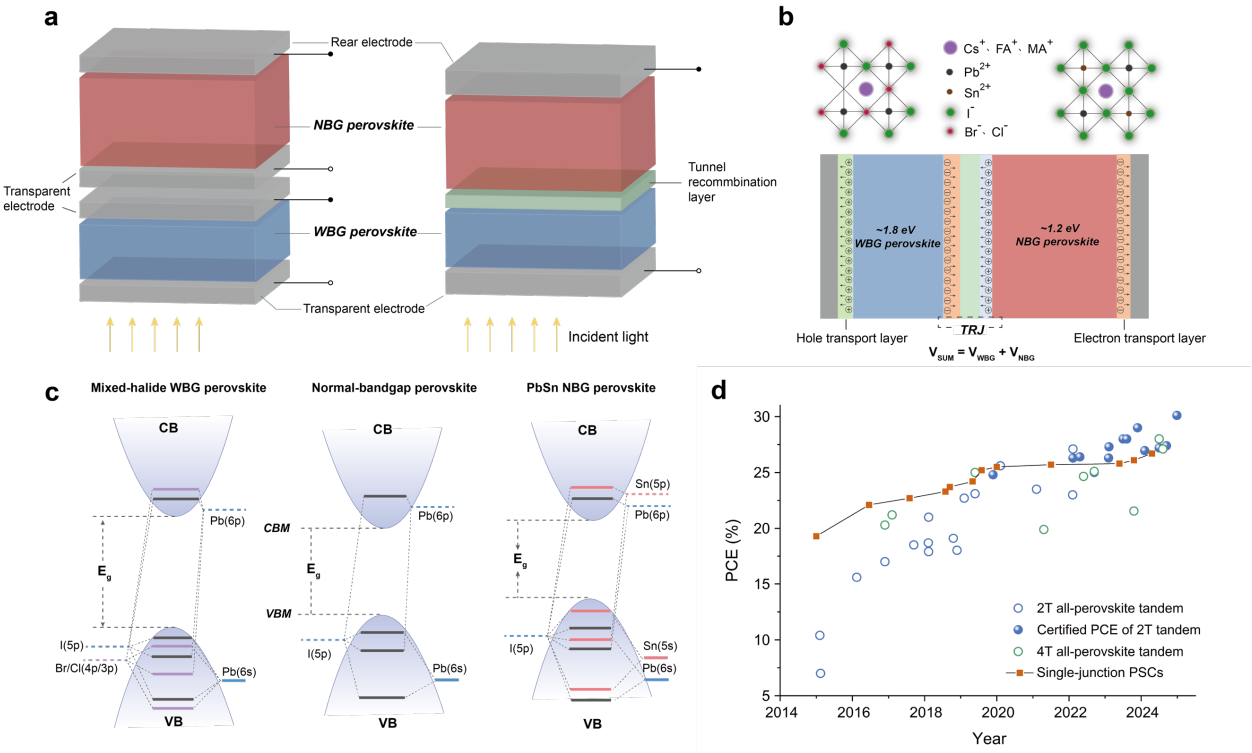


**Fig.1| Structures and working principles of all-perovskite tandem solar cells. a,** The classification of all-perovskite tandem devices into 2T and 4T configurations. **b,** Perovskite materials and working principles of 2T all-perovskite tandem solar cell. **c,** A schematic illustration of how ion doping modifies the bandgap and energy levels of perovskite materials. **d,** A comparison of the efficiency progress of 2T and 4T all-perovskite tandem solar cells against single-junction counterparts. Solid dots represent certified efficiencies, while hollow dots represent non-certified efficiencies.

The tunability of the perovskite's bandgap allows for each of the subcells to achieve current match in a 2T tandem architecture. In $ABX_3$-type perovskites, as shown in **Fig. 1c**, the bandgap is governed by the hybridization of B-site cation orbitals with X-site anion orbitals[6]. Modifying these sites allows desired bandgaps. For 2T tandem solar cells, wide-bandgap (WBG, ~1.8 eV) perovskites are achieved through halide composition adjustments at the X-site, while Sn doping at the B-site produces the narrow-bandgap (NBG, down to ~1.2 eV) perovskites, expanding the utilization of the near-infrared solar spectrum efficiently[7].

Research on 2T tandem architecture has gained considerable attraction, with rapid performance advancements. The certified efficiencies for 2T tandems have now exceeded 30%, far surpassing those of single-junction perovskite solar cells (26.7%) and 4T tandems (28.0%)[8] (**Fig. 1d**). Given the rapid progress and significant potential for commercialization, this review focuses on the advancements and challenges associated with 2T all-perovskite tandem solar cells and modules.

## Strategies to exceed single junction efficiency limit

The recent efficiency advancements in all-perovskite tandem solar cells have been mainly driven by two key factors: innovations in TRJs (**Fig. 2**) and improvements in both WBG and NBG subcells (**Fig. 3a**). These breakthroughs were primarily rooted in an enhanced understanding of the p-i-n architecture of perovskite solar cells (PSCs), which has enabled significant efficiency gains in both subcells. Key factors contributing to these gains encompass: a significant reduction in non-radiative defects in the absorber layers, optimized surface passivation treatments, and improved charge-carrier transport layers to enhance the electron- or hole-extraction/transport properties, while suppressing surface recombination at that interface. (**Fig. 3b and 3c**).

**BOX 2| Performance evolution of all-perovskite tandem solar cells and modules**

The figure illustrates the evolution of all-perovskite tandem solar cells and modules, focusing on key advancements in PCE and stability from 2016 to 2025. The development can be categorized into three distinct phases:

Early studies on all-perovskite tandem solar cells focused on finding suitable TRJ architectures and improving the crystallization of NBG subcells. Initial designs used the sputtered ITO as the TRJ and atomic layer deposition (ALD)-$SnO_x$ as a buffer layer, achieving a PCE of 16.9%[9]. Subsequent advancements came to incorporating the evaporated $MoO_x$ into Ag/ITO interfaces and chlorides ($Cl^-$) into NBG perovskites, increasing PCEs to over 21%[10]. Later, ALD-deposited $SnO_2$ layers paired with ultrathin Au nanoclusters created efficient TRJs, simplifying fabrication and enabling certified efficiencies of up to 24.8% in 2019[11]. This TRJ design has since become a mainstream choice for high-efficiency tandem architecture. However, at this stage, the operational stability ($T_{90}$ represents the time required to degrade to 90% of the initial efficiency) of tandem devices remained below 500 h[11].

Efforts shifted to enhancing crystallinity and reducing defects in the perovskite absorber layer of each subcells to boost tandem performance since 2020. Key innovations included incorporating 4-trifluoromethyl-phenylammonium ($CF_3$-PA) into Pb-Sn perovskite precursors, extending carrier diffusion length, and achieving a certified tandem efficiency of 26.4% with $T_{90}$ stability of 600 h[12]. Gentle gas-quenching methods controlled mixed-halide WBG crystallization, yielding a $V_{OC}$ of 1.33 V, tandem efficiencies of 27.1%, and $T_{80}$ stability of 1,825 h[13]. For tandem modules, the optimized WBG compositions enabled large-area fabrication with a module efficiency of 22.5% and a $T_{80}$ stability of 500 h[14].

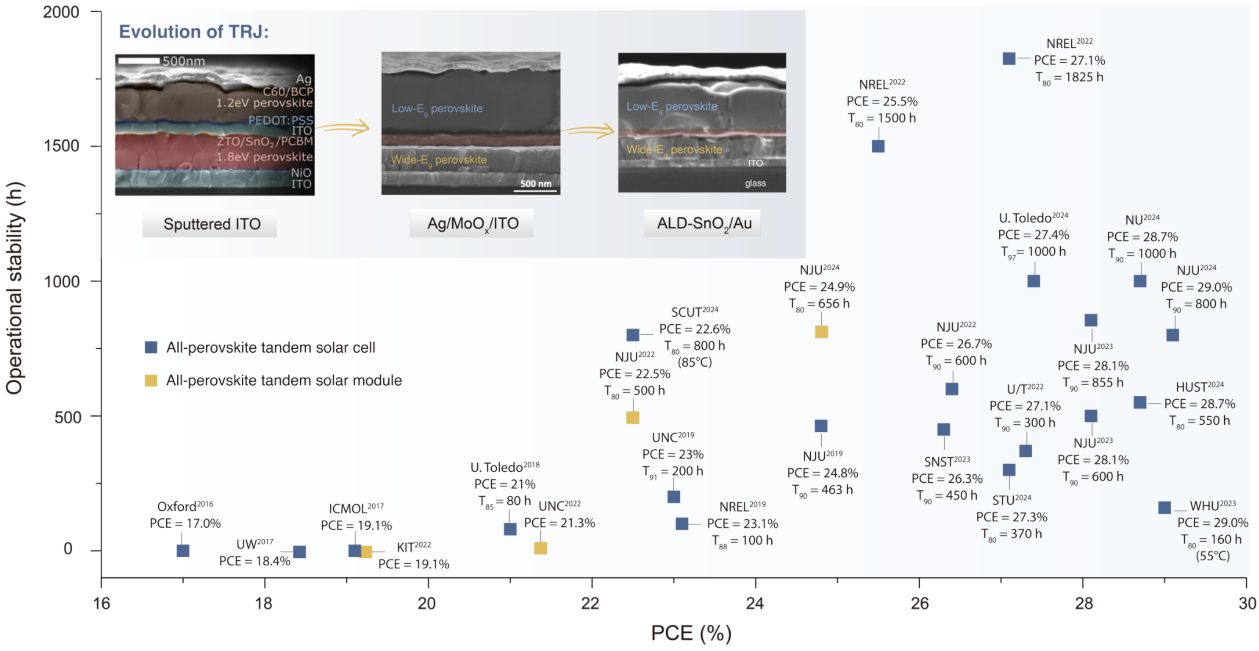


**Fig.2| The statistic efficiencies and operational stabilities of tandem devices.** Blue squares represent small-size devices below 1 cm², and yellow squares represent mini-modules beyond 10 cm$^2$. The inset illustrates the evolution of TRJ structures in tandem devices[9–11].

Research focused on interfaces between the perovskite and their respective hole or electron-transport layers (HTLs or ETLs) since 2022. These advances lead to a reduction in surface defects and improved energy level alignment, which contribute to improvements in both efficiency and stability. For WBG subcells, diammonium molecules were used to enhance surface states, achieving uniform surface potential and a tandem efficiency of 27.4%[15]. Advanced 3D/3D heterojunction in NBG subcells reduced non-radiative recombination and improved charge extraction ability, enabling tandem efficiencies exceeding 28% with $T_{90}$ stability approaching 1,000 h[16]. Tandem modules also experienced significant progress, achieving efficiencies up to ~25%

through advanced crystallization of NBG perovskite and enhanced passivation at the buried interface, achieving $T_{80}$ stability beyond 600 h[17].

**Unique issues in NBG perovskites subcell**

NBG perovskites present distinct challenges compared to Pb-based perovskites, particularly due to the oxidation of $Sn^{2+}$ to $Sn^{4+}$, resulting in an additional Sn vacancy ($V_{Sn}$) defects[18] (**Fig. 3d**). This oxidation is visually evident with a color change in the precursor solution and can also occur through more subtle mechanisms, such as solvent-mediated and charge-induced oxidation. To address these issues, several redox-based strategies have been developed. Comproportionation, utilizing metallic Sn to reduce $Sn^{4+}$ to $Sn^{2+}$ in the precursor solution, extends the charge-carrier diffusion length in Pb-Sn perovskites and achieves PCEs exceeding 21%[11] (**Fig. 3e**). Amphiphilic antioxidants with surface-anchoring properties, such as formamidinium sulfonic acid (FSA), enhanced film uniformity, yielding a PCE of 21.7%[19]. Additionally, electron-withdrawing ligands like chloromethyl phosphonic acid (CMP) mitigated Sn oxidation[20], reducing defect density and achieving efficiencies of 21.65% with a $V_{OC}$ of 0.852 V.

Driven by the high Lewis acidity of $Sn^{2+}$ and its fast coordination with organic components, the rapid crystallization of NBG perovskites pose significant challenges in fabricating high-quality films. This process often produces small grains with high-density grain boundaries that might act as nonradiative recombination centers and trap sites (**Fig. 3f**). Additionally, Sn alloying induces grain contraction, leading to residual strain that exacerbates defect formation and hinders charge extraction. The weak Sn-I bonding compared to Pb-I further causes organic cation depletion at the film surface, increasing the trap density. Key innovations have focused on optimizing charge transport and defect passivation to address these issues. Incorporating $CF_3$-PA into the precursor solution significantly extended the carrier diffusion length to over 5 μm, enabling the fabrication of thicker NBG perovskite layers (up to 1.2 μm)[12]. This advancement improved the short-circuit current density ($J_{SC}$) and efficiencies exceeding 22% for NBG subcell, contributing to a certified tandem efficiency of 26.4% that surpassed those of single-junction perovskite solar cells for the first time.

Another noteworthy approach involves introducing quasi-two-dimensional (quasi-2D) structures, such as $(PEA)_2GAPb_2I_7$, by using mixed bulky organic cations like phenethylammonium ($PEA^+$) and guanidinium ($Gua^+$)[22]. These structures effectively passivated defects and enhanced the

structural and optoelectronic properties of 1.25-eV Pb-Sn perovskites. These advancements addressed crystallization-induced defects and charge transport limitations, enabling NBG subcell efficiencies exceeding 22% and tandem cell efficiencies up to 25.5%.

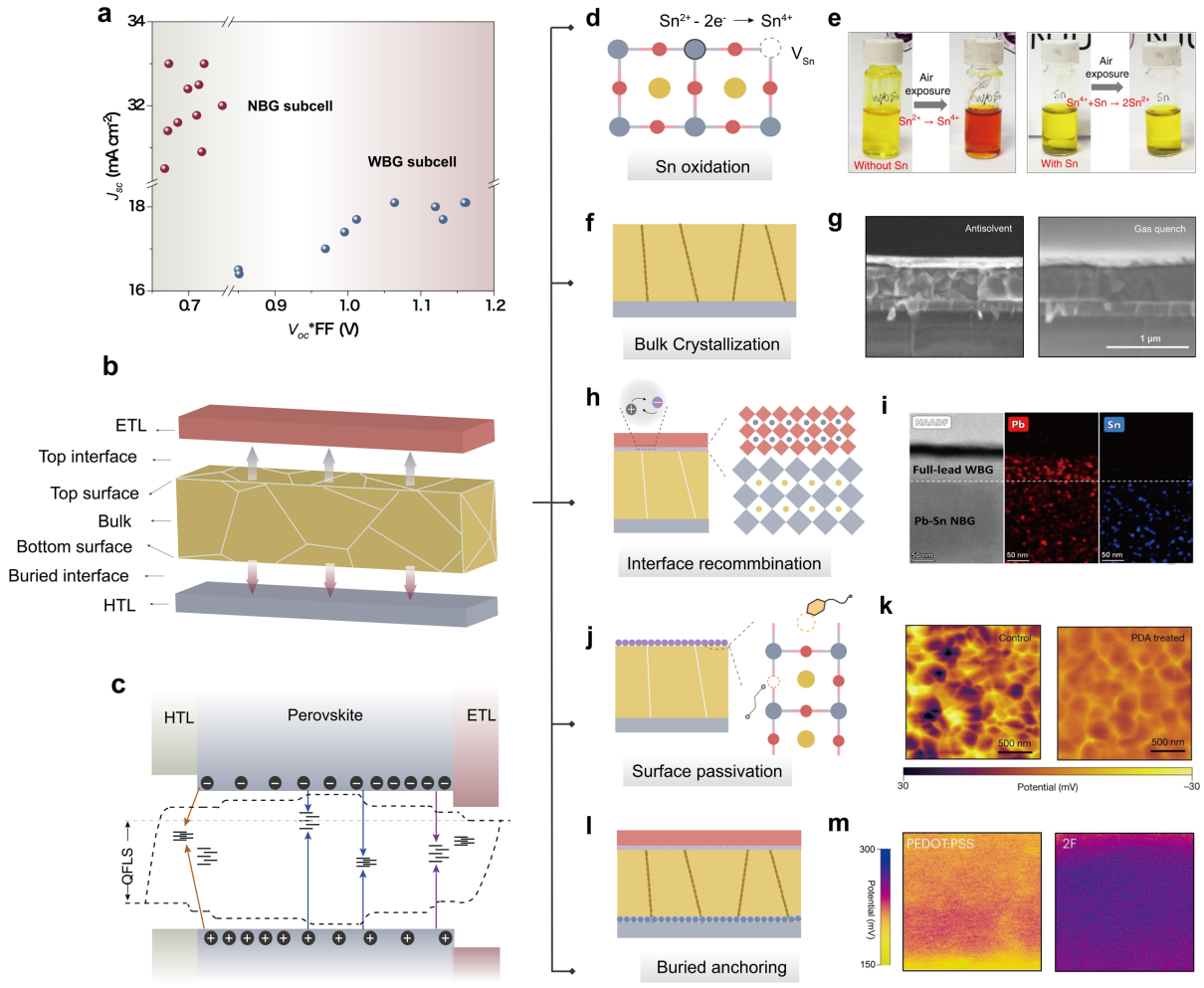


**Fig.3| Strategies to enhance efficiency in WBG and NBG subcells. a,** Statistical performance parameters of WBG and NBG perovskite sub-cells in tandem configuration. **b,** Sources of performance losses in p-i-n architecture of PSCs. **c,** Non-radiative recombination pathways in devices. **d,** The issue of $Sn^{2+}$ oxidation in NBG sub-cells. **e,** Photographs showing the ease of oxidation of $Sn^{2+}$ to $Sn^{4+}$ in ambient air and the facile reduction of $Sn^{4+}$ to $Sn^{2+}$ by metallic Sn powders[11]. **f,** Schematic diagram of perovskite bulk crystallization regulation and grain boundary passivation. **g,** Cross-section scanning electron microscope (SEM) images of WBG perovskite films made with antisolvent and gas-quench methods[13]. **h,** Schematic diagram of molecular passivation on the perovskite surface. **i,** Kelvin probe force microscopy (KPFM) images of control and PDA-treated WBG films[15]. **j,** Schematic diagram of heterojunction formation at the perovskite interface. **k,** Cross-sectional high-resolution scanning transmission electron microscopy (HR-STEM) image and corresponding

energy-dispersive X-ray (EDX) mapping of Pb-Sn PSCs with bilayer perovskite heterojunction[16]. **l,** Schematic diagram of HTL improvement and buried passivation anchoring in devices. **m,** KPFM images of different NBG perovskite films deposited on PEDOT:PSS and MPA2FPh-BT-BA (2F)[21].

## Unique issues in WBG perovskites

For WBG perovskite subcells, the experimentally reported $V_{OC}$ have consistently fallen short of theoretical maximums compared to normal-bandgap devices[23]. Recent advancements in understanding the underlying causes of $V_{OC}$ losses have shifted the focus beyond just phase segregation due to high bromide (Br) content. While phase segregation remains a critical issue for long-term stability (discussed in the next part), the increased $V_{OC}$ in WBG perovskite films is often linked to deep trap states induced by halide interstitials[24]. A higher Br content can amplify the formation of transient hole traps, adversely impacting quasi-fermi level splitting (QFLS) and thus photoluminescence quantum yields (PLQY)[25] (**Fig. 3c**). Density functional theory studies have shown that halide interstitials are thermodynamically stable and contribute significantly to the formation of deep trap states[26]. Advanced characterization techniques such as photoemission electron microscopy and multimodal operando microscopy have been developed to enable nanoscale mapping and spatial correlation of charge transport losses, recombination losses, and chemical composition, providing critical insights into the spatial heterogeneity within perovskite films and the origins of performance limitations[27,28]. Non-radiative recombination pathways are particularly pronounced at grain boundaries and surfaces in perovskite films, which is driven by the complex crystallization kinetics of mixed cations and halides.

Addressing the above challenges requires strategies to either homogenize the crystallization process or effectively passivate surface and bulk defects. Notably, gas quenching has been highly effective for producing components with higher cesium ($Cs^+$) content, resulting in an improved structural quality and higher $V_{OC}$[13,29,30](**Fig. 3g**). A promising approach involves a film-side-down close-space annealing (CSA) process, in which solvent release was precisely controlled, resulting in high-quality perovskite absorbers with micrometer-scale grains and prolonged carrier lifetimes[31]. For WBG perovskites, additive strategies such as incorporating 2D passivation, chloride or pseudohalide-based salts, and multifunctional small molecules have been employed to regulate film morphology and reduce defect states. Despite these advancements, the inherent crystalline heterogeneity of WBG materials still results in more significant losses compared to the highly crystalline quality of $FAPbI_3$ films, underscoring the need for further exploration and refinement.

**Interface engineering in p-i-n structure**

Following reducing bulk defects, strategies have increasingly focused on reducing non-radiative recombination between the perovskite and HTL or ETL interfaces. High-density traps at perovskite heterojunction interfaces, often formed by unpassivated dangling bonds, are among the primary causes of recombination losses[32]. By tailoring the terminal groups at the perovskite interface, surface modification effectively reduces defects and further improves charge extraction.

**Perovskite-ETL interface**

Various surface modification techniques have substantially improved the performance of p-i-n PSCs by addressing two critical aspects: (1) forming heterojunctions to induce n-type properties in the top surface region, facilitating efficient charge transfer (**Fig. 3h**), and (2) reducing surface defects to minimize recombination losses (**Fig. 3j**). For instance, strategies to create a type-II band alignment at the Pb-Sn perovskite/ETL interface have been employed to suppress the undesired p-type doping concentration, reduce defect-induced surface recombination velocity (SRV), and improve electron extraction[16] (**Fig. 3i**). These approaches have enabled Pb-Sn perovskite solar cells with 1.2-μm-thick absorbers and thus achieving high PCE of 23.8%, with a $V_{OC}$ of 0.873 V and a FF of 82.6%[16]. Further research has revealed that mixed Pb-Sn perovskite films often exhibit compositional gradients with excess Sn at the top surface, leading to oxidation and accelerated recombination rates[33]. Diamines have been used to chelate Sn atoms to address this issue, achieving a more balanced Sn stoichiometry. This strategy forms a low-resistance barrier layer that passivates defects, enabling efficiencies of up to 23.9% in NBG devices.

Optimizing the perovskite/ETL interface has also improved $V_{OC}$ and FF in WBG subcells for tandem architecture. Three main strategies have been developed: (1) anchoring functional materials on the perovskite surface and constructing (2) low-dimensional or (3) heterostructured materials atop the perovskite absorber. Organic salts like guanidinium bromide (GuaBr), phenethylammonium iodide (PEAI), butylammonium bromide (BABr), and 4-(trifluoromethyl)phenylethylammonium are widely used as passivation to stabilize the perovskite surface and reduce non-radiative recombination losses[34–36]. Co-modifiers like diammonium combined with methylthio or phenylethylammonium molecules have also demonstrated selective passivation for defect states, reducing trap-assisted recombination in both WBG and NBG perovskites[37,38] (**Fig. 3k**). A recent strategy using a mixture of MAI and PEAI in the anti-solvent

enabled the fabrication of WBG perovskites with enhanced (100) plane orientation, achieving a certified tandem PCE over 29%. This method promotes 2D ($n$ = 1) layered perovskite formation, oriented nucleation, and downward crystal growth, reducing non-radiative recombination in the bulk and interfaces. In addition to organic interface engineering, ultrathin dipole layers, such as $MgF_2$ or LiF, inserted at the perovskite/$C_{60}$ interface mitigated non-radiative recombination and enhanced device performance[39].

**Perovskite-HTL interface**

The buried perovskite/HTL interface poses a significant challenge for p-i-n PSCs. High density of deep trap states at this interface have been revealed through mechanical and chemical delamination methods[40,41](**Fig. 3l**). Advances in HTLs, such as replacing traditional PEDOT:PSS with multifunctional materials like MPA2FPh-BT-BA (2F, **Fig. 3m**), have led to improved energy level alignment, regulated perovskite growth, and effective defect passivation[21]. Since 2022, self-assembled monolayers (SAMs) anchored on transparent conductive oxide (TCO) or nickel oxide ($NiO_x$) as HTLs have emerged as a mainstream HTLs in WBG subcells, replacing traditional conductive polymers like (poly[bis(4-phenyl) (2,4,6-trimethyl-phenyl)amine) (PTAA) and N4,N4′-di(naphthalen-1-yl)-N4,N4′-bis(4-vinylphenyl)biphenyl-4,4′-diamine (VNPB)[42]. Early studies on SAMs, such as (2-(9H-carbazol-9-yl)ethyl)phosphonic acid (2PACZ) and Me-[4-(9H-carbazol-9-yl)butyl]phosphonic acid (Me-4PACz) demonstrated enhanced hole extraction and reduced interface traps, significantly reducing voltage losses in WBG devices. Subsequent development of SAMs, including (4-(7H-dibenzo[c,g]carbazol-7-yl)butyl)phosphonic acid (4PADCB), has further optimized the passivation efficacy, energy level alignment, and surface wettability, resulting in superior device performance[43].

Despite these advancements, the passivation of the buried interface has received less attention than the perovskite/ETL interface, mainly due to the solubility of passivation materials in perovskite precursor solvents. A doping strategy using chiral aspartate hydrochloride (AspCl) at the PEDOT interface was developed to address this limitation. This approach forms intermolecular hydrogen bonds throughout the perovskite film, enabling an efficiency of 22.46% in Pb-Sn perovskite solar cells[44]. Beyond doping HTLs with pre-embedded passivation molecules, studies have shown that large-size molecules preferentially settle to the bottom during crystallization, improving the quality of the underlying perovskite layer[45]. From another perspective, a vapor-solution two-step

method appears more suitable for bottom-surface passivation. However, this approach currently yields lower-quality perovskite films than the one-step spin-coating method, highlighting a need for further optimization.

## Operational stability of all-perovskite tandem solar cells

As the efficiency of all-perovskite tandem solar cells surpasses the 30% benchmark, device stability becomes a critical issue, which is currently hindering their commercial potential. In recent years, significant progress has been made in enhancing the operational lifetimes of all-perovskite tandem solar cells (**Fig. 2**) through material design, crystallization regulation, defect passivation, and device structure optimization. Among these advancements, the most notable breakthroughs include mitigating halide segregation in WBG perovskites, optimizing the composition and structure of NBG perovskites, and developing robust interconnection layers. This section highlights these key developments and their role in advancing device stability.

### Light-induced halide segregation in WBG perovskites

WBG perovskites are more susceptible to halide segregation under continuous illumination, driven by photoinduced polarons and halogen ion migration[46,47]. This segregation forms I-rich and Br-rich regions, where photocarriers become trapped in low-bandgap I-rich domains, increasing non-radiative recombination loss. The phenomenon is further exacerbated by lattice defects, grain boundaries, and residual stress (**Fig. 4a**), underscoring the need for thermodynamically stable compositions and high-quality films.

Bulk strategies to address halide segregation focus on two main approaches: adjusting compositions to increase the activation energy for halide migration and reducing defects to suppress ion migration pathways (**Fig. 4b**). Recent studies have highlighted that halide segregation is not solely determined by Br content–the A-site cation also plays a significant role in the overall lattice structure[48,49]. While incorporating Cs enhances stability, it will introduce deep-level defects due to its size mismatch with formamidinium ($FA^+$). To mitigate this, larger A site cations (e.g., $DMA^+$, $Gua^+$, and $EA^+$) have been introduced to reduce lattice strain and defect densities[50,51]. At the X-site, $Cl^-$ doping has been shown to increase the halide migration barrier by alleviating lattice microstrain, thereby stabilizing the lattice framework[52]. A representative composition, $Cs_{0.4}FA_{0.5}DMA_{0.1}Pb(I_{0.72}Br_{0.23}Cl_{0.05})_3$, achieves a bandgap of 1.8 eV with an optimized PCE and improved photostability[29] (**Fig. 4c**).

Defects in WBG perovskite films act as low-energy pathways for ion migration, significantly reducing operational lifetimes. Theoretical studies indicate that phase segregation often originates at grain boundaries, where defect vacancies are concentrated[53]. Crystallization regulation strategies to address these issues have been covered in the previous section. Here, we highlight the critical role of interfaces in governing the photostability of WBG perovskite devices. Interfacial defects not only increase non-radiative recombination, thereby reducing efficiency but also lead to carrier accumulation within the perovskite layer, often resulting in irreversible degradation[54,55]. Studies have shown that under short-circuit conditions, where carrier accumulation is minimized, phase segregation in WBG perovskites is significantly suppressed[56]. In contrast, under open-circuit conditions, carrier accumulation can induce the formation of polarons, which amplify phase segregation and accelerate degradation[57]. This phenomenon explains the disparity between experimental observations of phase segregation occurring within minutes in thin films and the $T_{90}$ operational lifetimes of WBG devices, which can extend to several hundred hours under real-world conditions.

As the dominant HTLs in WBG subcells, SAMs can be further optimized by mixing multiple types to improve energy level alignment, enhance carrier collection, and ultimately boost the stability of WBG perovskite devices. However, their single-molecule anchoring mechanism can result in localized microscopic non-uniformity and susceptibility to solvent-induced detachmen[58,59]. Moreover, their long-term thermal stability remains uncertain, with potential risks of substrate delamination or desorption under prolonged stress. It is also worth exploring that the intrinsic stability of transport layers cannot be equated to their stability when integrated into devices. For example, while $NiO_x$ exhibits excellent intrinsic stability, their interfaces with perovskites often suffer from chemical reactions and significant defects, making them a primary source of degradation[60]. Striking a balance between these factors remains a key challenge for future research.

Incorporating thin, low-dimensional perovskite layers into top interfaces has enhanced stability, leveraging the hydrophobic nature of large organic cations and their higher ion migration barriers. However, conventional spin-coating methods often yield a 2D layer with $n$ =1 due to a solvent-driven surface-reconstruction displacement reaction. While $n$ =1 layers facilitate hole transport in n-i-p configurations, they impede electron transport at the $C_{60}$ interface in p-i-n architectures, diminishing the stability gains of the 2D layer. To address this, strategies such as solvent modulation during passivation, avoiding thermal annealing, and in situ formation of high-$n$ 2D

layers via evaporated $PbI_2$ have been developed[61–63]. These approaches improved energy level alignment and enhanced electron transport while optimizing stability and device performance, enabling the $T_{90}$ of WBG subcell to reach up to 1,700 h[57].

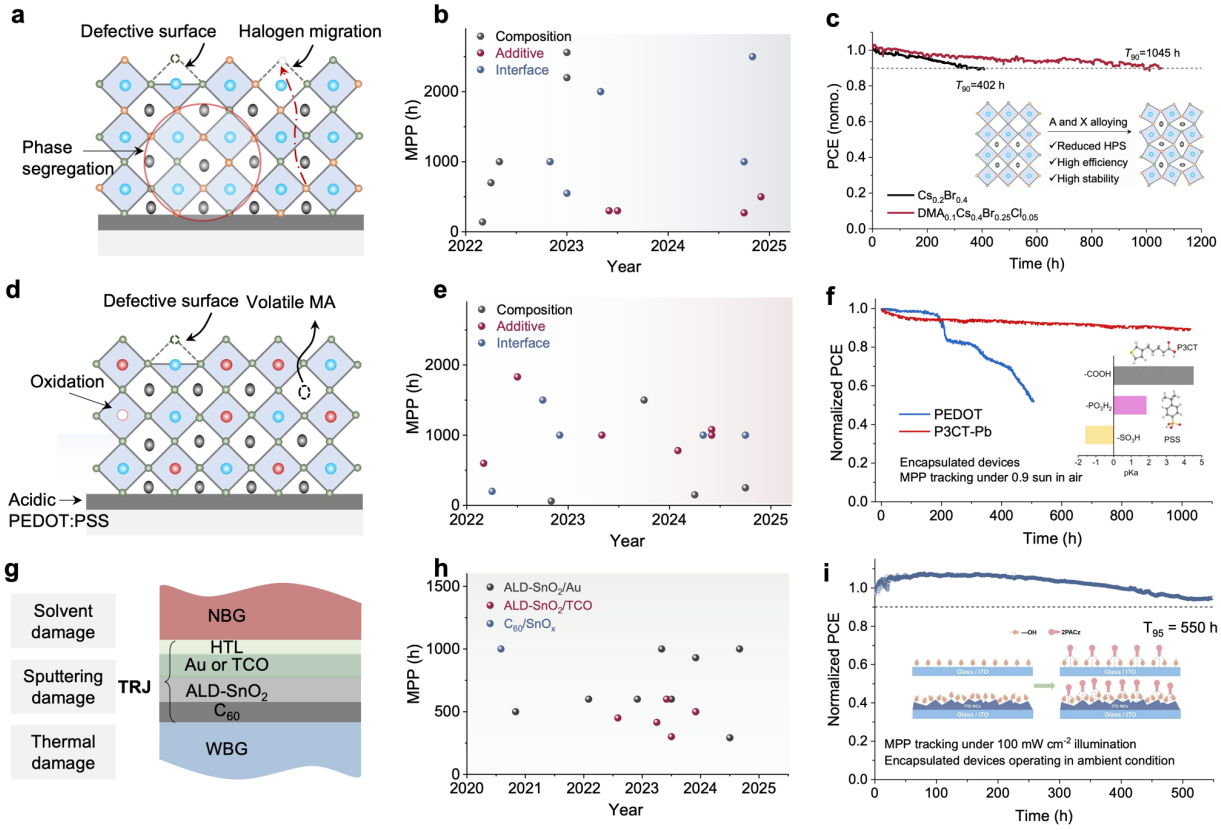


**Fig. 4| Operational stability of subcells and tandem PVs. a,** The stability issues of WBG perovskites. **b,** The summarized MPP statistics of WBG subcells. **c,** The MPP stability of WBG solar cells with A site and X site alloying[29]. **d,** The summarized stability issues of NBG perovskites. **e,** The summarized MPP statistics of NBG subcells. **f,** The MPP stability of NBG solar cells with P3CT HTL[64]. **g,** The stability issues of all-perovskite tandem solar cells originating from TRJ. **h,** The summarized MPP statistics of all-perovskite solar cells with different TRJ. **i,** The MPP stability of the art-of-the-state all-perovskite tandem solar cells with a TRJ structure of SnO2/NC-ITO/SAMs[75].

## Stability issues in NBG perovskites

The oxidation of $Sn^{2+}$ and the rapid crystallization leading to high defect states (**Fig. 4d**), discussed in the efficiency section, are also strongly linked to stability and are not reiterated extensively here. Although methylammonium ($MA^+$) ions have been shown to enhance stability in specific scenarios, their inclusion at levels exceeding 30% in high-efficiency NBG compositions poses considerable

stability risks. The volatility, hygroscopicity, and thermal instability of $MA^+$ significantly compromise device durability, particularly under elevated temperatures such as the 85°C conditions specified in IEC standards (**Fig. 4d**). To address these issues, pure FA-based Pb-Sn perovskites were developed, achieving efficiencies of 21.0% in single-junction cells and 26.3% in all-perovskite tandem, with $T_{90}$ of 212 h thermal stability at 85°C under dark[66]. Incorporating Cs into FA-based systems further enhanced thermal robustness, giving rise to double- and triple-cation compositions such as FACs and FARbCs[67]. These systems demonstrated improved resistance to light and humidity, with stabilized efficiencies and significant gains in long-term operational stability. For instance, advanced RbCsFA compositions have achieved a record efficiency of 24.13% and thermal stability $T_{90}$ of 795 h[68]. All-inorganic $CsPb_{0.4}Sn_{0.6}I_3$ perovskites have also shown promise, offering superior thermal stability, with $T_{80}$ exceeding 1,510 h at 65°C and 800 at 85°C, despite relatively lower efficiencies of 17.4%[69]. These results highlight the potential for further optimization of inorganic compositions.

The acidity of PEDOT:PSS, a commonly used HTL, negatively impacts device stability. Modifications to PEDOT:PSS, such as p-guanidinobenzonitrile hydrochloride treatment, have improved performance, achieving a PCE of 23.3% with a $T_{80}$ of 300 h[70]. Exploring alternatives to PEDOT:PSS is a valuable direction. Additives like multifunctional ammonium sulfide (MAS)[71], oxalic acid (OA)[72], and acetylcholine chloride (ACh) have been used to modify PEDOT:PSS[73], achieving PCE over 24% in NBG subcell. These strategies have also demonstrated efficiencies of ~28% with a $T_{80}$ of 500 h under MPP conditions for all-perovskite tandem. SAMs are another promising approach for Pb-Sn devices, yielding a PCE of 23.46% with a $T_{88}$ of 590 hours at 65°C[43]. Impressively, $GeI_2$-modified $NiO_x$ achieved a PCE of 23.34% with storage stability exceeding 4,320 h in $N_2$[74]. A novel HTL, P3CT, with a higher $pK_a$, overcame interface degradation and enabled tandem to retain 96% of their initial PCE after >1,000 h of MPP testing under ambient conditions (**Fig. 4f)**, representing the best stability performance to date for this device type[64].

**Stability issues from interconnection layer**

While the $SnO_2$/ultra-thin Au/PEDOT:PSS configuration is the mainstream TRJ structure for all-perovskite tandem, concerns about the scalability of this design arise due to the potential interfacial diffusion of Au clusters during prolonged operation (**Fig. 4g** and **4h**).. To address these concerns, various interconnection layer innovations have been proposed to enhance stability. One promising

alternative is the $SnO_2$/NC-ITO/SAMs structure, which combines high transparency and excellent electrical conductivity[66,75]. The NC-ITO layer was fabricated using a low-temperature solution-processing method, reducing damage to the underlying subcells and demonstrating superior stability with $T_{95}$ of 550 h[75] (**Fig. 4i)**. Another widely used TRJ configuration is the $SnO_2$/sputtered-TCO/PEDOT structure, where sputtered TCO films such as ITO and IZO provide high transparency and conductivity[4365]. In perovskite-organic tandem cells, a sputtered IZO layer sandwiched between BCP or $SnO_x$ and $MoO_x$ has achieved record PCEs of 24% by minimizing optical and electrical losses[76,77]. However, the sputtering process, particularly at high temperatures or with high-energy particles, risks irreversible damage to the underlying perovskite subcell and limiting its adoption in high-efficiency all-perovskite tandem devices.

A novel approach employs an n-$SnO_2$/p-$SnO_{2-x}$ TRJ, leveraging the bipolar properties of $SnO_x$ for efficient electron and hole transport[65]. The simplified $C_{60}$/$SnO_{2-x}$ interconnection layer further improves the efficiency and photostability of 2T all-perovskite tandems by reducing reliance on complex TRJ structures and minimizing sputtering-induced damage However, the need for precise control of pulse and reaction times to achieve the optimal Sn:O ratio has hindered its widespread application.

**Perspective for stability research**

Stability research for tandem devices lags behind that for single-junction cells, with most studies limited to ISOS-L1 protocols and 85°C thermal tests. To identify instability sources, tandem devices face unique challenges requiring broader tests, such as ISOS-D-3 (85°C, 85% humidity), bias stability, and mechanical stress assessments. At the module level, outdoor testing is essential to evaluate real-world degradation factors. Advanced in-situ tools like photoelectron microscopy and synchrotron radiation will be critical for providing dynamic, high-resolution insights into perovskite behavior under operational conditions.

While efficiency improvements in perovskite devices have progressed rapidly, stability analysis remains more complex and time-intensive. Strategies such as introducing additives or interface treatments often enhance efficiency but do not always improve stability, highlighting the need for tailored approaches. Looking ahead, high-throughput research methods integrated with machine learning could redefine stability studies. By enabling large-scale data collection and analysis, these

approaches may help identify molecular candidates that simultaneously enhance stability and efficiency, accelerating material and device optimization.

## Challenges and Innovations in Upscaling Production

Most all-perovskite tandem PSCs reported with high PCEs are based on lab-scale small area (<1 $cm^2$) in 2T architecture (**Fig. 1d)**, which stimulated scaling up to over 1-$cm^2$ area and even mini-module dimension of >10 $cm^2$ (**Fig. 5a**). In this section, we focus on the upscaling of 2T all-perovskite tandem devices. Improving PCEs of large-area all-perovskite tandem devices by scalable methods is challenging, since upscaling from small area to large size induces new complexities, such as sequential scalable processing, film homogeneity, interfacial quality, charge transport/collection, and module designs.

### Upscaling of over 1 $cm^2$ tandem solar cells

The early stage of upscaling all-perovskite tandem achieved a PCE of approximately 24% by employing a novel hole transport layer, $NiO_x$/VNPB, and using FSA to regulate the crystallization of NBG perovskites[19]. In 2023, ~1 $cm^2$ tandem solar cells benefited from a significant research momentum of SAM HTL in WBG perovskite subcell[43] (**Fig. 5b**), pushing PCEs up to >26% with enhanced $V_{OC}$ of >2.1 eV. Compared to ~0.1 $cm^2$ small-area devices, ~1 $cm^2$ tandem solar cells suffer severe PCE loss due to surficial inhomogeneity, especially at the perovskite/ETL interface. Recently, several novel strategies achieved uniform passivation, such as forming 3D/3D or 2D/3D bilayer perovskite heterojunction (using thermal evaporation), Dion-Jacobson or Ruddlesden-Popper 2D phases, realizing a groundbreaking certified PCE up to 28.2% on ~1 $cm^2$ area[78]. These breakthroughs narrowed the absolute PCE gap to <1.5% for upscaling from ~0.1 to ~1 $cm^2$ levels, providing promising pathways to large-sized module fabrication.

### Scalable processing of tandem solar modules

Scaling up perovskite films to large-area module dimensions necessitates moving beyond spin coating to scalable and cost-effective methods such as slot-die coating, blade coating, thermal evaporation, spray coating, and inkjet printing. The currently reported high-efficiency devices are all prepared using the blade-coating method (**Fig. 5b**). Functional layers, including charge transport layers and TRJs, can be deposited using techniques like thermal evaporation, blade coating, ALD, and sputtering.

The development of all-perovskite tandem solar modules has lagged behind single-junction solar modules and small-area (<1 cm²) tandem solar cells (**Fig. 5b**). Only a few prototypes have been demonstrated to date[14,17,79–81], reflecting the significant challenges in transitioning to fully scalable processing for large-area substrates. Sequential deposition of multiple layers (>10) and the control of perovskite crystallization for both WBG and NBG layers are critical hurdles. Additionally, transitioning from spin-coating to scalable techniques and scaling up from ~1 cm² to module-sized areas present significant barriers to achieving high performance (**Fig. 5b**).

Despite these challenges, advancements in module design and scalable coating technologies have enabled an all-perovskite tandem solar mini-module to achieve a certified aperture-area PCE of 24.5%, surpassing the current record of 23.2% for single-junction solar mini-modules. The following sections will explore the key factors driving this performance improvement.

**Key parameters of efficiency losses for modules**

The module $V_{OC,module}$ is the sum of the $V_{OC}$ of all sub-cells. $V_{OC,module}$ loss mainly originates from the scalable coating quality of the large-area perovskite layer that is dominated by morphological homogeneity, crystal quality, thickness uniformity, and interfacial quality. The module short-circuit current ($I_{SC,module}$) is determined by the smallest $I_{SC}$ of sub-cell. $I_{SC,module}$ loss is mainly associated with geometric fill factor (GFF, i.e., the proportion of active area to aperture area, **Fig. 5c**) and internal series resistance ($R_S$) of the entire module.

P1 and P3 scribes isolate, while P2 scribes connect adjacent sub-cell electrodes. Accurate control of P2 scribe width is crucial; excessively wide scribes decrease the GFF, and overly narrow ones increase resistive losses due to incomplete layer removal, TCO damage, debris redistribution, or metal-halide interactions[82] (**Fig. 5c**). A thin conformal diffusion barrier layer, i.e., ~10 nm ALD-$SnO_x$, was employed after P2 scribing process to prevent the interfusion between Ag electrode and $I^-$, simultaneously forming good ohmic contact with low vertical resistance at the ITO/ALD-$SnO_2$/Ag junction and also improving the device stability[14]. This also isolated Ag and PEDOT:PSS in the recombination junction, enhancing shunt resistance. Optimized laser scribing (e.g., pulse energy, frequency, and speed) ensures uniform ablation, complete layer removal, and avoids TCO damage. Additionally, air-exposure degradation, particularly in NBG perovskites, must be addressed during module fabrication.

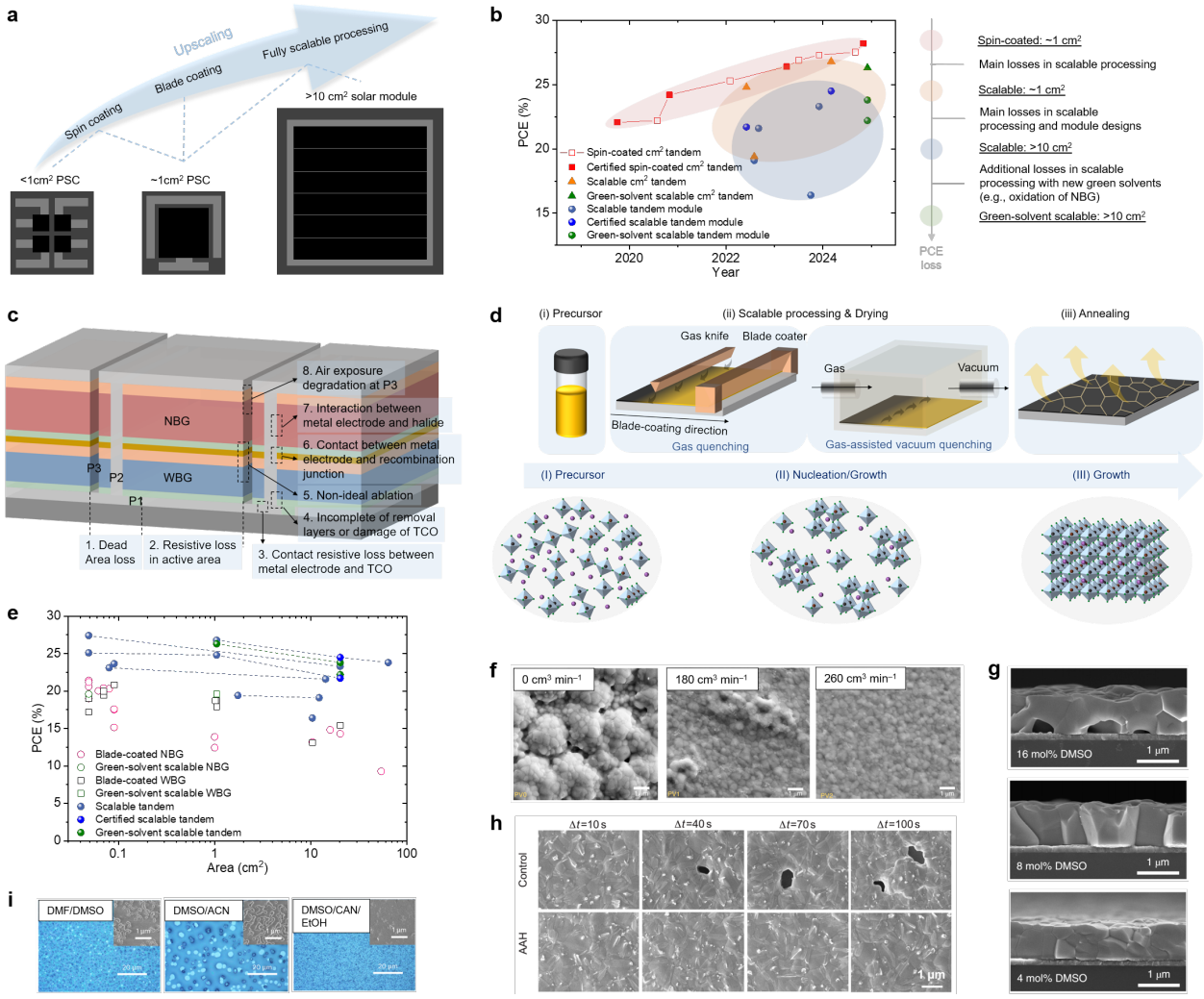


**Fig.5| Upscaling fabrication of all-perovskite tandem. a,** Illustration of upscaling from small-area (<1 $cm^2$, spin coating) to large-area (~1 $cm^2$, spin coating, blade coating, or fully scalable processing) and module dimension (>10 $cm^2$, fully scalable processing). **b**, PCE evolution of ~1 $cm^2$ all-perovskite PSCs and min-modules. **c**, Schematic illustration of all-perovskite solar modules with series interconnection and summarized possibilities of geometrical losses in module designs. **d**, Schematic illustration of scalable processing of large-area perovskite films and key control of crystallization. **e**, PCE progress of single-junction and all-perovskite tandem PSCs or modules based on blade-coating process. **f**, SEM images of the NBG perovskite films fabricated using vacuum-quenching process in combination with different $N_2$ flow[81] (PV0: 0 $cm^3$ $min^{-1}$; PV1: 180 $cm^3$ $min^{-1}$; PV2: 260 $cm^3$ $min^{-1}$). **g**, Cross-section SEM images of the blade-coated NBG perovskite films using different molar ratio (referred to Pb and Sn) of DMSO in the precursor[79]. **h**, SEM images of the blade-coated NBG perovskite films (with and without additive of aminoacetamide hydrochloride (AAH)) at different processing window ($\Delta t$)[17]. **i**, Microscopy photographs and SEM images (inset) of peeled-off WBG perovskite films (i.e., the morphology of the buried interface) using different solvent system in the precursor[80].

**Control of perovskite crystallization in scalable processing**

Perovskite film quality and homogeneity are controlled by crystallization kinetics that involves a classical theory of nucleation and crystal growth (**Fig. 5d**). In general, two pathways involve in the first step: homogeneous (*i.e.*, the nuclei generated within the precursor without any preferential sites) and heterogeneous nucleation (*i.e.*, the nuclei preferentially form in specific regions, such as on the substrate surface, at defect sites, or around impurities)[88].

One of the critical challenges is the inherent uncontrollable rapid crystallization of Sn-based perovskites that induces complexity and difficulty in the blade-coating process[89]. The higher Lewis acidity of $Sn^{2+}$ and lower solubility of $SnI_2$ (in DMF/DMSO solvent system) make the crystallization conditions more stringent and induce a narrow processing window, *e.g.*, Sn-based perovskites are capable of crystallizing at room temperature, unlike Pb-based perovskites requiring post-annealing. In addition, the difference in dynamic crystallization kinetics and thermodynamic stability creates competition between Sn and Pb, resulting in an inhomogeneous distribution throughout the perovskite film (e.g., imbalanced stoichiometry of Sn and Pb). Therefore, the uncontrollable properties of rapid crystallization generally led to poor homogeneity, increased defect density, and low crystalline quality. These also explain scalable processing of NBG perovskite films is currently a key production bottleneck for the advancement of all-perovskite solar modules (**Fig. 5e**). A moderate nitrogen flow (260 $cm^3$ $min^{-1}$) was employed for fabricating 12.25 $cm^2$ NBG perovskite film, resulting in an accelerated mass transport from the NBG perovskite surface and improved crystallization. It produced a uniform morphology free of defects and pinholes (**Fig. 5f**), achieving a PCE of 19.1% in scalable mini-modules[81]. To blade coat a thick (~1 μm) NBG perovskite film, the as-fabricated wet film also required to be thick. However, the trapped DMSO (high boiling-point solvent) near the buried interface induces the interfacial voids due to the top-to-bottom crystallization direction[17,79]. To avoid the void formation, the reduced molar ratio of DMSO (optimum of 8%, referred to Pb and Sn) was utilized in the precursor, resulting in enlarged grain sizes and void-free buried interface[79] (**Fig. 5g**). This enabled efficient all-perovskite tandem solar modules delivering a PCE of 21.6% over a 14.3 $cm^2$ aperture area. It is also found that the wettability of NBG perovskite becomes worse on top of large-area PEDOT:PSS substrate with the decay of coating time, leading to non-uniform nuclei density subsequent to uneven solvent extraction. Therefore, it is crucial to extend the processing window of blade coating as it is a time-demanding step. A novel additive AAH was employed to retard the

crystallization as it coordinates strongly with precursor. The processing window was extended up to 100 s without performance loss due to high homogeneity and quality of NBG perovskite films[17] (**Fig. 5h**). AAH was also demonstrated accumulation at the buried interface with passivating defects. Fully scalable all-perovskite tandem solar modules achieved a certified PCE of 24.5% with 20.25 $cm^2$ aperture area (**Fig. 5b**). This approach also reached a high PCE of 23.8% with 64 $cm^2$ aperture area (**Fig. 5e**). Recently, the same group released a record certified PCE of 24.8% over 64 $cm^2$ aperture area[1].

Scalable processing of WBG perovskite films remains challenging. Mixed-halide WBG perovskites exhibit diverse crystallization kinetics, often accompanied by phase heterogeneity issues[14,87]. Additionally, Cs and Br salts have limited solubility in polar aprotic solvents, such as DMF and DMSO. These constrain the scalable processing of large-area WBG perovskite films for module production. In response, the nucleation was controlled by varying the Cs content. The optimized composition of $Cs_{0.35}FA_{0.65}PbI_{1.8}Br_{1.2}$ realized enlarged grain sizes, improved film homogeneity, and reduced phase segregation[14]. A certified PCE of 21.7% was achieved in mini-modules (**Fig. 5e**). Some additives (such as methylammonium thiocyanate[88] and glycine amide hydrochloride[96]) were also employed for regulating crystallization in the blade-coating process. Very recently, green-solvent scalable fabrication was developed in all-perovskite tandem solar modules. For replacing DMF, a green solvent system composed of DMSO/acetonitrile (ACN)/ethyl alcohol (EtOH) was developed to extend the processing window and avoid void formation at the buried interface[80] (**Fig. 5i**). With utilizing green solvents in WBG perovskite precursor, a high PCE of 23.8% was reached in the tandem modules. The green solvent system was also demonstrated upscaling capability in NBG perovskite fabrication. As a result, the mini-module based on fully green solvents for processing of both WBG and NBG perovskites realized a PCE of 22.2% (Fig. 5e). The PCE gap (**Fig. 2b**) was attributed to the $Sn^{2+}$ oxidation caused by DMSO as a higher ratio of DMSO was used in green solvent system[92]. The achievement opens the door for environmentally friendly production of all-perovskite tandem modules.

## Perspective and outlooks

As highlighted in the previous section, all-perovskite tandem solar cells have garnered significant research interest in recent years. This section will discuss potential directions for future exploration, key challenges, and outlooks.

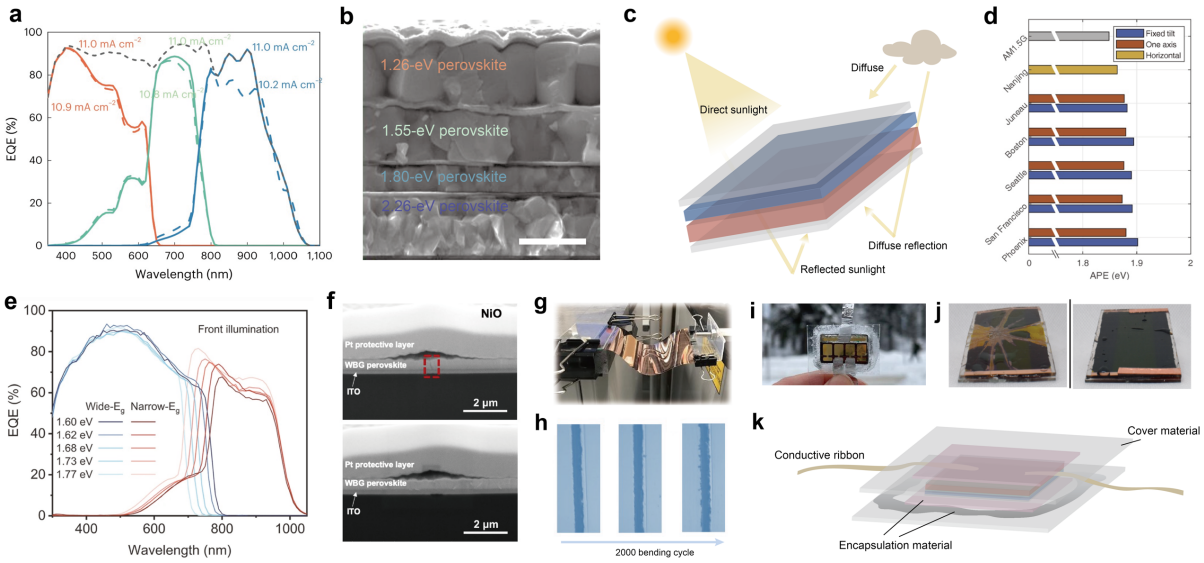


**Fig.6| Prospect of all-perovskite tandem PV. a,** External quantum efficiency (EQE) spectra of the triple-junction device using propane-1,3-diiodide additive[89]. **b,** Cross-sectional SEM image of the all-perovskite quadruple-junction cell[90]. Scale bar, 1 μm. **c,** Light absorption, including direct, diffused and reflected sunlight, from the surrounding environment of a bifacial tandem device. **d,** The annual weighted average solar spectral irradiance of six cities[91]. **e,** EQE curves of WBG and NBG subcells in bifacial all-perovskite tandems with various top-cell bandgaps under front (glass) side illumination[92]. **f,** Cross-sectional SEM images of flexible WBG PSCs with NiO and MB-NiO after 10000 bending cycles with a bending radius of 10 mm[93]. **g,** The photos of bending test of flexible module under bending[94]. **h,** Microscopy images of laser-scribed P3 on the minimodules before and after 2000 bending[94]. **i,** Photo of one-step coating encapsulation[95]. **j,** Photos of perovskite modules after hail impact testing[96]. **k,** Schematic diagram of perovskite device encapsulation.

## Multi-junction configurations for enhanced efficiency

Multi-junction architectures represent transformative strategies for surpassing the efficiency limits of tandem devices by harnessing a broader portion of the solar spectrum[97] (**Fig. 6a** and **6b**). Unlike the high-cost III-V multi-junction cells, perovskite-based multi-junction solar cells offer a cost-effective and high-performance alternative for terrestrial applications. Recent advances have demonstrated efficiencies exceeding 27% for triple- and quadruple-junction PVs[90], yet leaving significant gaps remaining to the practical efficiency potential of 37%[98] (for ideal bandgaps of 1.2/1.5/2.0 eV).

These differences between theoretical and experimental efficiencies are primarily attributed to the performance limitations in WBG (2.0 eV) top cells, where high Br content complicates film quality.

Due to the versatility of WBG cells, the optimization of all-perovskite multijunction devices often aligns with advancements in perovskite/Si and perovskite/organic multijunction technologies. Emerging strategies to overcome these challenges include the use of halogenated diammonium salts and propane-1,3-diiodide as additives to enhance halide homogeneity. Compositional engineering—such as replacing $Cs^+$ with $Rb^+$ at the A-site and introducing halogenocyanate ($OCN^-$) at the X-site—has shown promise in alleviating lattice strain[99]. Very recently, a new benchmark for multi-junction PV was achieved by enhancing Pb-Sn perovskite films with amino acid salts, which synergistically improved film quality and optoelectronic properties, leading to record PCEs of 28.7% for triple-junction and 27.9% for quadruple-junction devices[90](**Fig. 6b**). Realizing the full potential of multi-junction will require continued optimization of subcell performance, complemented by advanced light management techniques, including anti-reflective coatings and photonic structures, to ensure optimal photon utilization and current matching.

**Real-world optimization with structure design**

The real-world performance of all-perovskite tandem PVs depends on adapting to variables such as tilt angles, tracking methods, and climatic factors, including solar spectra and humidity. Considering albedo irradiation in realistic irradiation conditions, the bifacial tandem PV retains a higher energy yield gain compared to the monofacial PV[100]. For bifacial tandem modules, effective light management becomes critical to achieve current matching and maximize energy capture from both direct and diffuse light (**Fig. 6c**). Advanced strategies such as bandgap tuning[92] (**Fig. 6e**), angular response optimization, and thermal management systems are being developed to address these challenges.

A key hurdle under field test conditions (FTCs) is "current mismatch", where varying angles of incidence (AOI) and spectral shifts disrupt subcell photocurrent balance. Unlike the controlled conditions of standard test protocols, FTCs expose devices to dynamic thermal effects, wind, and humidity, which can alter perovskite bandgaps and exacerbate mismatch. Despite these challenges, tandem PVs have demonstrated the ability to outperform single-junction devices under diffuse light and non-standard spectra[91](**Fig. 6d**), highlighting their potential for superior field performance.

All-perovskite tandem flexible modules, combining high efficiency with mechanical adaptability, are well-suited for wearable electronics, curved surfaces, and building-integrated PVs. However,

achieving long-term operational stability under mechanical stress, environmental exposure, and thermal cycling remains a formidable challenge. Studies have shown that replacing $NiO_x$ with $NiO_x$/SAM transport layers significantly enhances mechanical resilience[93] (**Fig. 6f**). Further progress will require optimizing intermediate TRJ structures to balance electrical performance with bending flexibility, as well as mitigating delamination and thermal effects induced by laser scribing. For instance, bending-induced metal delamination along P3 grooves remains a critical issue, increasing the risk of short circuits[94] (**Fig. 6g** and **6h**). Addressing these limitations is essential for advancing the reliability and scalability of flexible tandem modules.

**Environmental lifecycle enhancement**

The environmental footprint of all-perovskite tandem solar cells is a critical consideration for their large-scale adoption. Future industrialization should prioritize transitioning to fully green solvent-based or evaporation-based fabrication methods. Encapsulation plays a dual role: it ensures long-term device stability and serves as a vital barrier against Pb leakage during operation. Current encapsulation techniques include single-layer coatings, such as UV-curable epoxy resin or silicone (**Fig. 6i**), and multi-step hot pressing using thermoplastic polymers (**Fig. 6j** and **6k**). Among these, multi-step hot pressing is widely employed in industrial settings due to its robust protective capabilities, though it necessitates further innovation to enhance efficiency and flexibility while minimizing efficiency losses during the heating process. Future advancements should focus on developing high-performance multilayer barrier films, advanced adhesive interfaces, and innovative flexible encapsulation designs.

Despite the many challenges that remain in realizing the full potential of all-perovskite multi-junction devices, the sustained effort and rapid progress in perovskite research offer a promising outlook. We strongly believe that all-perovskite tandems present the ultimate embodiment of perovskite technology, paving the way for the development of highly efficient and cost-effective thin-film modules, and ultimately driving their large-scale manufacturing and deployment.

## References


1. Green, M. A. *et al.* Solar Cell Efficiency Tables (Version 65). *Prog. Photovoltaics Res. Appl.* 1–13 (2024) doi:10.1002/pip.3867.
2. Aydin, E. *et al.* Pathways toward commercial perovskite/silicon tandem photovoltaics. *Science.* **383**, 1–13 (2024).
3. Marti, A. & Araújo, G. L. Limiting efficiencies for photovoltaic energy conversion in multigap systems. *Sol. Energy Mater. Sol. Cells* **43**, 203–222 (1996).
4. Jošt, M., Kegelmann, L., Korte, L. & Albrecht, S. Monolithic Perovskite Tandem Solar Cells: A Review of the Present Status and Advanced Characterization Methods Toward 30% Efficiency. *Adv. Energy Mater.* **10**, 1904102 (2020).
5. Ko, Y., Park, H., Lee, C., Kang, Y. & Jun, Y. Recent Progress in Interconnection Layer for Hybrid Photovoltaic Tandems. *Adv. Mater.* **32**, 2002196 (2020).
6. Brivio, F., Walker, A. B. & Walsh, A. Structural and electronic properties of hybrid perovskites for high-efficiency thin-film photovoltaics from first-principles. *APL Mater.* **1**, (2013).
7. Walsh, A. Principles of chemical bonding and band gap engineering in hybrid organic-inorganic halide perovskites. *J. Phys. Chem. C* **119**, 5755–5760 (2015).
8. Li, G. *et al.* Boosting All-Perovskite Tandem Solar Cells by Revitalizing the Buried Tin-Lead Perovskite Interface. *Adv. Mater.* **36**, 2401698 (2024).
9. Eperon, G. E. *et al.* Perovskite-perovskite tandem photovoltaics with optimized band gaps. *Science.* **354**, 861–865 (2016).
10. Zhao, D. *et al.* Efficient two-terminal all-perovskite tandem solar cells enabled by high-quality low-bandgap absorber layers. *Nat. Energy* **3**, 1093–1100 (2018).
11. Lin, R. *et al.* Monolithic all-perovskite tandem solar cells with 24.8% efficiency exploiting comproportionation to suppress Sn(ii) oxidation in precursor ink. *Nat. Energy* **4**, 864–873 (2019).
12. Lin, R. *et al.* All-perovskite tandem solar cells with improved grain surface passivation. *Nature* **603**, 73–78 (2022).
13. Jiang, Q. *et al.* Compositional texture engineering for highly stable wide-bandgap perovskite solar cells. **1300**, 1295–1300 (2023).
14. Xiao, K. *et al.* Scalable processing for realizing 21.7%-efficient all-perovskite tandem solar modules. *Science.* **376**, 762–767 (2022).
15. Chen, H. *et al.* Regulating surface potential maximizes voltage in all-perovskite tandems. *Nature* **613**, 676–681 (2023).
16. Lin, R. *et al.* All-perovskite tandem solar cells with 3D/3D bilayer perovskite heterojunction. *Nature* **620**, 994–1000 (2023).
17. Gao, H. *et al.* Homogeneous crystallization and buried interface passivation for perovskite tandem solar modules. *Science.* **383**, 855–859 (2024).

18. Chung, I. *et al.* CsSnI3: semiconductor or metal? High electrical conductivity and strong near-infrared photoluminescence from a single material. High hole mobility and phase-transitions. *J. Am. Chem. Soc.* **134**, 8579–8587 (2012).

19. Xiao, K. *et al.* All-perovskite tandem solar cells with 24.2% certified efficiency and area over 1 cm2 using surface-anchoring zwitterionic antioxidant. *Nat. Energy* **5**, 870–880 (2020).

20. Yu, D. *et al.* Electron-withdrawing organic ligand for high-efficiency all-perovskite tandem solar cells. *Nat. Energy* **9**, 298–307 (2024).

21. Zhu, J. *et al.* A donor–acceptor-type hole-selective contact reducing non-radiative recombination losses in both subcells towards efficient all-perovskite tandems. *Nat. Energy* **8**, 714–724 (2023).

22. Tong, J. *et al.* Carrier control in Sn–Pb perovskites via 2D cation engineering for all-perovskite tandem solar cells with improved efficiency and stability. *Nat. Energy* **7**, 642–651 (2022).

23. Oliver, R. D. J. *et al.* Understanding and suppressing non-radiative losses in methylammonium-free wide-bandgap perovskite solar cells. *Energy Environ. Sci.* **15**, 714–726 (2022).

24. Mahesh, S. *et al.* Revealing the origin of voltage loss in mixed-halide perovskite solar cells. *Energy Environ. Sci.* **13**, 258–267 (2020).

25. Stolterfoht, M. *et al.* How To Quantify the Efficiency Potential of Neat Perovskite Films: Perovskite Semiconductors with an Implied Efficiency Exceeding 28%. *Adv. Mater.* **32**, 2000080 (2020).

26. Hörantner, M. T. & Snaith, H. J. Predicting and optimising the energy yield of perovskite-on-silicon tandem solar cells under real world conditions. *Energy Environ. Sci.* **10**, 1983–1993 (2017).

27. Macpherson, S. *et al.* Local nanoscale phase impurities are degradation sites in halide perovskites. *Nature* **607**, 294–300 (2022).

28. Frohna, K. *et al.* The impact of interfacial quality and nanoscale performance disorder on the stability of alloyed perovskite solar cells. *Nat. Energy* (2024) doi:10.1038/s41560-024-01660-1.

29. Wen, J. *et al.* Steric Engineering Enables Efficient and Photostable Wide-Bandgap Perovskites for All-Perovskite Tandem Solar Cells. *Adv. Mater.* **34**, 2110356 (2022).

30. Ternes, S., Laufer, F. & Paetzold, U. W. Modeling and Fundamental Dynamics of Vacuum, Gas, and Antisolvent Quenching for Scalable Perovskite Processes. *Adv. Sci.* **11**, 2308901 (2024).

31. Wang, C. *et al.* A universal close-space annealing strategy towards high-quality perovskite absorbers enabling efficient all-perovskite tandem solar cells. *Nat. Energy* **7**, 744–753 (2022).

32. Isikgor, F. H. *et al.* Molecular engineering of contact interfaces for high-performance perovskite solar cells. *Nat. Rev. Mater.* **8**, 89–108 (2023).

33. Li, C. *et al.* Diamine chelates for increased stability in mixed Sn–Pb and all-perovskite tandem solar cells. *Nat. Energy* **9**, 1388–1396 (2024).

34. Yang, G. *et al.* Stable and low-photovoltage-loss perovskite solar cells by multifunctional passivation. *Nat. Photonics* **15**, 681–689 (2021).

35. Caprioglio, P. *et al.* Open-circuit and short-circuit loss management in wide-gap perovskite p-i-n solar cells. *Nat. Commun.* **14**, 932 (2023).

36. Liu, Z. *et al.* Reducing perovskite/C60 interface losses via sequential interface engineering for efficient perovskite/silicon tandem solar cell. *Adv. Mater.* **36**, 2308370 (2024).

37. Wang, X. *et al.* Highly efficient perovskite/organic tandem solar cells enabled by mixed-cation surface modulation. *Adv. Mater.* **35**, 2305946 (2023).

38. Liu, C. *et al.* Bimolecularly passivated interface enables efficient and stable inverted perovskite solar cells. *Science.* **382**, 810–815 (2023).

39. Liu, J. *et al.* Efficient and stable perovskite-silicon tandem solar cells through contact displacement by MgF x. *Science.* **377**, 302–306 (2022).

40. Yang, X. *et al.* Buried Interfaces in Halide Perovskite Photovoltaics. *Adv. Mater.* **33**, 2006435 (2021).

41. Xiao, T. *et al.* Elimination of grain surface concavities for improved perovskite thin-film interfaces. *Nat. Energy* **9**, 999–1010 (2024).

42. Al-Ashouri, A. *et al.* Monolithic perovskite/silicon tandem solar cell with >29% efficiency by enhanced hole extraction. *Science.* **370**, 1300–1309 (2020).

43. He, R. *et al.* Improving interface quality for 1-cm2 all-perovskite tandem solar cells. *Nature* **618**, 80–86 (2023).

44. Zhou, S. *et al.* Aspartate all-in-one doping strategy enables efficient all-perovskite tandems. *Nature* **624**, 69–73 (2023).

45. Hu, S. *et al.* Optimized carrier extraction at interfaces for 23.6% efficient tin–lead perovskite solar cells. *Energy Environ. Sci.* **15**, 2096–2107 (2022).

46. Hoke, E. T. *et al.* Reversible photo-induced trap formation in mixed-halide hybrid perovskites for photovoltaics. *Chem. Sci.* **6**, 613–617 (2015).

47. Barker, A. J. *et al.* Defect-Assisted Photoinduced Halide Segregation in Mixed-Halide Perovskite Thin Films. *ACS Energy Lett.* **2**, 1416–1424 (2017).

48. Beal, R. E. *et al.* Structural Origins of Light-Induced Phase Segregation in Organic-Inorganic Halide Perovskite Photovoltaic Materials. *Matter* **2**, 207–219 (2020).

49. Mcmeekin, D. P. *et al.* A mixed-cation lead mixed-halide perovskite absorber for tandem solar cells. *Science.* **351**, 151–156 (2016).

50. Palmstrom, A. F. *et al.* Enabling Flexible All-Perovskite Tandem Solar Cells. *Joule* **3**, 2193–2204 (2019).

51. Huang, Z. *et al.* Stable, Bromine-Free, Tetragonal Perovskites with 1.7 eV Bandgaps via A-Site Cation Substitution. *ACS Mater. Lett.* **2**, 869–872 (2020).

52. Xu, J. *et al.* Triple-halide wide-band gap perovskites with suppressed phase segregation for efficient tandems. *Science.* **367**, 1097–1104 (2020).

53. Tang, X. *et al.* Local Observation of Phase Segregation in Mixed-Halide Perovskite. *Nano Lett.* **18**, 2172–2178 (2018).

54. Ahn, N. *et al.* Trapped charge-driven degradation of perovskite solar cells. *Nat. Commun.* **7**, 1–9 (2016).

55. Khenkin, M. V., Anoop, K. M., Katz, E. A. & Visoly-Fisher, I. Bias-dependent degradation of various solar cells: Lessons for stability of perovskite photovoltaics. *Energy Environ. Sci.* **12**, 550–558 (2019).

56. Lin, Y. *et al.* Excess charge-carrier induced instability of hybrid perovskites. *Nat. Commun.* **9**, 4981 (2018).

57. Wen, J. *et al.* Heterojunction formed via 3D-to-2D perovskite conversion for photostable wide-bandgap perovskite solar cells. *Nat. Commun.* **14**, 7118 (2023).

58. Park, S. M. *et al.* Low-loss contacts on textured substrates for inverted perovskite solar cells. *Nature* **624**, 289–294 (2023).

59. Tang, H. *et al.* Reinforcing self-assembly of hole transport molecules for stable inverted perovskite solar cells. *Science.* **383**, 1236–1240 (2024).

60. Elnaggar, M. *et al.* Decoupling Contributions of Charge-Transport Interlayers to Light-Induced Degradation of p-i-n Perovskite Solar Cells. *Sol. RRL* **4**, 1–10 (2020).

61. Azmi, R. *et al.* Damp heat–stable perovskite solar cells with tailored-dimensionality 2D/3D heterojunctions. *Science.* **376**, 73–77 (2022).

62. Chen, H. *et al.* Quantum-size-tuned h eterostructures enable efficient and stable inverted perovskite solar cells. *Nat. Photonics* **31**, 1903559 (2022).

63. Choi, H. *et al.* A Review on Reducing Grain Boundaries and Morphological Improvement of Perovskite Solar Cells from Methodology and Material-Based Perspectives. *Small Methods* **4**, 1900569 (2020).

64. Fu, S. *et al.* Suppressed deprotonation enables a durable buried interface in tin-lead perovskite for all-perovskite tandem solar cells. *Joule* **8**, 2220–2237 (2024).

65. Yu, Z. *et al.* Simplified interconnection structure based on C60/SnO2-x for all-perovskite tandem solar cells. *Nat. Energy* **5**, 657–665 (2020).

66. Wu, P. *et al.* Efficient and Thermally Stable All-Perovskite Tandem Solar Cells Using All-FA Narrow-Bandgap Perovskite and Metal-oxide-based Tunnel Junction. *Adv. Energy Mater.* **12**, 2202948 (2022).

67. Alsulami, A. *et al.* Triiodide Formation Governs Oxidation Mechanism of Tin-Lead Perovskite Solar Cells via A-Site Choice. *J. Am. Chem. Soc.* **146**, 22970–22981 (2024).

68. Zhang, Y. *et al.* Synchronized crystallization in tin-lead perovskite solar cells. *Nat. Commun.* **15**, 6887 (2024).

69. Duan, C. *et al.* Durable all inorganic perovskite tandem photovoltaics. *Nature* 0–1 (2024) doi:10.1038/s41586-024-08432-7.

70. He, D. *et al.* Synergistic Passivation of Buried Interface and Grain Boundary of Tin–Lead Mixed Perovskite Films for Efficient Solar Cells. *Adv. Funct. Mater.* **2411750**, 1–9 (2024).

71. Song, J. *et al.* Multifunctional Ammonium Sulfide Enables Highest Efficiency Lead–Tin Perovskite Solar Cells. *Adv. Funct. Mater.* **2411746**, 1–8 (2024).

72. Zhu, J. *et al.* Custom-tailored hole transport layer using oxalic acid for high-quality tin-lead perovskites and efficient all-perovskite tandems. *Sci. Adv.* **10**, 1–10 (2024).

73. Li, G. *et al.* Boosting All-Perovskite Tandem Solar Cells by Revitalizing the Buried Tin-Lead Perovskite Interface. *Adv. Mater.* **36**, 2401698 (2024).

74. Lee, S. *et al.* Unprecedented inorganic HTL-based MA-free Sn–Pb perovskite photovoltaics with an efficiency over 23%. *Energy Environ. Sci.* **17**, 8140–8150 (2024).

75. Liu, C. *et al.* Efficient All-Perovskite Tandem Solar Cells with Low-Optical-Loss Carbazolyl Interconnecting Layers. *Angew. Chemie - Int. Ed.* **62**, 1–9 (2023).

76. Chen, W. *et al.* Monolithic perovskite/organic tandem solar cells with 23.6% efficiency enabled by reduced voltage losses and optimized interconnecting layer. *Nat. Energy* **7**, 229–237 (2022).

77. Brinkmann, K. O. *et al.* Perovskite–organic tandem solar cells with indium oxide interconnect. *Nature* **604**, 280–286 (2022).

78. Wang, Y. *et al.* Homogenized contact in all-perovskite tandems using tailored 2D perovskite. *Nature* **635**, 867–873 (2024).

79. Dai, X. *et al.* Efficient monolithic all-perovskite tandem solar modules with small cell-to-module derate. *Nat. Energy* **7**, 923–931 (2022).

80. Duan, C. *et al.* Scalable fabrication of wide-bandgap perovskites using green solvents for tandem solar cells. *Nat. Energy* (2024) doi:10.1038/s41560-024-01672-x.

81. Abdollahi Nejand, B. *et al.* Scalable two-terminal all-perovskite tandem solar modules with a 19.1% efficiency. *Nat. Energy* **7**, 620–630 (2022).

82. Park, N. G. & Zhu, K. Scalable fabrication and coating methods for perovskite solar cells and solar modules. *Nat. Rev. Mater.* **5**, 333–350 (2020).

83. Zhu, P. *et al.* Toward the Commercialization of Perovskite Solar Modules. *Adv. Mater.* **36**, 2307357 (2024).

84. Yin, M. *et al.* A Revisit of Crystallization in Tin Halide Perovskite Thin Films: From Nucleation, Intermediate to Crystal Growth. *Adv. Funct. Mater.* **2404792**, 1–37 (2024).

85. Wang, Z. *et al.* Manipulating the crystallization kinetics of halide perovskites for large-area solar modules. *Commun. Mater.* **5**, 131 (2024).

86. Hu, S. *et al.* Narrow Bandgap Metal Halide Perovskites for All-Perovskite Tandem Photovoltaics. *Chem. Rev.* **124**, 4079–4123 (2024).

87. Fang, H. *et al.* Efficient Blade-Coated Wide-Bandgap and Tandem Perovskite Solar Cells via a Three-Step Restraining Strategy. *Adv. Mater.* 2414790 (2024) doi:10.1002/adma.202414790.

88. Zhou, X. *et al.* Suppressing Nonradiative Losses in Wide-Band-Gap Perovskites Affords Efficient and Printable All-Perovskite Tandem Solar Cells with a Metal-Free Charge Recombination Layer. *ACS Energy Lett.* **8**, 502–512 (2023).

89. Wang, J. *et al.* Halide homogenization for low energy loss in 2-eV-bandgap perovskites and increased efficiency in all-perovskite triple-junction solar cells. *Nat. Energy* **9**, 70–80 (2023).

90. Hu, S. *et al.* Steering perovskite precursor solutions for multijunction photovoltaics. *Nature* (2024) doi:10.1038/s41586-024-08546-y.

91. Gao, Y. *et al.* Performance optimization of monolithic all-perovskite tandem solar cells under standard and real-world solar spectra. *Joule* **6**, 1944–1963 (2022).

92. Li, H. *et al.* Revealing the output power potential of bifacial monolithic all-perovskite tandem solar cells. *eLight* **2**, 21 (2022).

93. Li, L. *et al.* Flexible all-perovskite tandem solar cells approaching 25% efficiency with molecule-bridged hole-selective contact. *Nat. Energy* **7**, 708–717 (2022).

94. Xu, W. *et al.* Multifunctional entinostat enhances the mechanical robustness and efficiency of flexible perovskite solar cells and minimodules. *Nat. Photonics* **18**, 379–387 (2024).

95. Mousavi, S. M. *et al.* Addressing the efficiency loss and degradation of triple cation perovskite solar cells via integrated light managing encapsulation. *Mater. Today Energy* **46**, 101707 (2024).

96. Zhang, G. *et al.* Shellac protects perovskite solar cell modules under real-world conditions. *Joule* **8**, 496–508 (2024).

97. Wang, Z. *et al.* Suppressed phase segregation for triple-junction perovskite solar cells. *Nature* **618**, 74–79 (2023).

98. Hörantner, M. T. *et al.* The Potential of Multijunction Perovskite Solar Cells. *ACS Energy Lett.* **2**, 2506–2513 (2017).

99. Liu, S. *et al.* Triple-junction solar cells with cyanate in ultrawide-bandgap perovskites. *Nature* **628**, 306–312 (2024).

100. Gota, F., An, S. X., Hu, H., Abdollahi Nejand, B. & Paetzold, U. W. Energy Yield Modeling of Bifacial All-Perovskite Two-Terminal Tandem Photovoltaics. *Adv. Opt. Mater.* **11**, 2201691 (2023).

## Acknowledgment

H.T. and J.W. acknowledge financial support from the National Key R&D Program of China (2022YFB4200304), the National Natural Science Foundation of China (T2325016, U21A2076, 61974063, 62125402, 62321166653, 62305150), the Natural Science Foundation of Jiangsu Province (BE2022021, BE2022026, BK20202008, BK20190315, BK20232022), the Fundamental Research Funds for the Central Universities (0213/14380206, 0205/14380252), the Frontiers

Science Center for Critical Earth Material Cycling Fund (DLTD2109), the "GeoX" Interdisciplinary Research Funds for the Frontiers Science Center for Critical Earth Material Cycling at Nanjing University, and the Program for Innovative Talents and Entrepreneurs in Jiangsu. H.H. and U.W.P. acknowledge funding partly provided by the European Union (ERC Consolidator Grant, Lami-Pero, 101087673). Views and opinions expressed are, however, those of the authors only and do not necessarily reflect those of the European Union or the European Research Council Executive Agency. Neither the European Union nor the granting authority can be held responsible for them. J.T. acknowledges funding from the National Key R&D Program of China (2023YFB3608900). C.C. acknowledges support from the Innovation Project of Optics Valley Laboratory (OVL2024ZD002). D.P.M. and H.J.S. are funded by the European Union. Views and opinions expressed are, however, those of the author(s) only and do not necessarily reflect those of the European Union or the Research and Innovation Agency (RIA). Neither the European Union nor the granting authority can be held responsible for them. The NEXUS project has received funding from the European Union's Horizon Europe research and innovation program under grant agreement No. 101075330. Additional support is acknowledged from the program grants funded by the Engineering and Physical Science Research Council (EPSRC), including ATIP (EP/T028513/1) and HEFSPV (EP/V027131/1).

## Competing interests

Hairen Tan is the founder, Chief Scientific Officer, and Chairman of Renshine Solar Co., Ltd., a company that is commercializing perovskite PVs. H.J.S. is the co-founder and CSO of Oxford PV Ltd. The other authors declare no competing financial or non-financial interests.